INL/JOU-21-63056-Revision-0

Microstructural characterization of as-fabricated monolithic plates with boron carbide, aluminum boride, and zirconium boride burnable absorbers

Jordan Andrew Evans, Dennis D Keiser Jr, Adam B Robinson, Irina Glagolenko, Jan-Fong Jue, Curtis R Clark, Ashley E. Paz y Puente

Changing the World's Energy Future

Idaho National Laboratory

INL is a U.S. Department of Energy National Laboratory operated by Battelle Energy Alliance, LLC

INL/JOU-21-63056-Revision-0

Microstructural characterization of as-fabricated monolithic plates with boron carbide, aluminum boride, and zirconium boride burnable absorbers

Jordan Andrew Evans, Dennis D Keiser Jr, Adam B Robinson, Irina Glagolenko, Jan-Fong Jue, Curtis R Clark, Ashley E. Paz y Puente

February 2022

Idaho National Laboratory
Idaho Falls, Idaho 83415

http://www.inl.gov

Prepared for the
U.S. Department of Energy
Under DOE Idaho Operations Office
Contract DE-AC07-05ID14517

Microstructural Characterization of As-Fabricated Monolithic Plates with Boron Carbide, Aluminum Boride, and Zirconium Boride Burnable Absorbers

Jordan A. Evans[1*], Ashley E. Paz y Puente[2], Adam B. Robinson[1], Irina Y. Glagolenko[1], Jan-Fong Jue[1], Curtis R. Clark[1], Yongho Sohn[3], Dennis D. Keiser Jr.[1]

[1] *Idaho National Laboratory, Idaho Falls, ID, 83415, USA*

[2] *University of Cincinnati, Cincinnati, OH, 45221, USA*

[3] *University of Central Florida, Orlando, FL, 32816, USA*

* Corresponding author.

Email addresses: Jordan.Evans@inl.gov (J. Evans), Ashley.PazyPuente@uc.edu (A. Puente), Adam.Robinson@inl.gov (A. Robinson), Irina.Glagolenko@inl.gov (I. Glagolenko), Jan-Fong.Jue@inl.gov (J. Jue), Curtis.Clark@inl.gov (C. Clark), Yongho.Sohn@ucf.edu (Y. Sohn), Dennis.Keiser@inl.gov (D. Keiser)

Abstract

The use of burnable absorbers can be beneficial for nuclear reactors by extending the fuel's operational cycle, providing additional criticality control, and flattening the power profile. In this work, three burnable absorber materials (boron carbide, aluminum boride, and zirconium boride) embedded in aluminum have been fabricated into foils and clad in AA-6061 for potential use in high performance research reactors. The as-fabricated boron-containing phases were determined using transmission electron microscopy to be AlB_2, B_4C, and ZrB_2. TEM also revealed incomplete bonding at the B_4C-matrix interface. SEM showed a relatively uniform spatial distribution of boron-containing phases for all the candidate materials. Higher porosity was observed in the foil containing ZrB_2 in its as-rolled condition. The porosity in the ZrB_2 foil was reduced by hot isostatic pressing. The size and shape distributions of the boron-containing phases were analyzed on the criteria of cross-sectional area, perimeter, roundness, circularity, and aspect ratio. A method of converting the 2D burnable absorber dispersoids seen in cross-sectional microscopy images into 3D volumes was derived using both spherical and ellipsoidal geometry models. The difference in calculated burnable absorber dispersoid average volume between the two models ranges from 20% to 100%, which could impact burnable absorber burnout rates due to differences in neutron self-shielding.

Nomenclature

2D	Two-dimensional

3D	Three-dimensional
σ	Standard deviation
A	Area
A_{3D}	Major axis length of the best-fit ellipsoid in the x direction
AA-6061	Aluminum alloy 6061
aLEU	Advanced low-enriched uranium
AR	Aspect ratio
ATR	Advanced Test Reactor
B&W	Black and white
B_{2D}	Major axis length of the best-fit ellipse
B_{3D}	Major axis length of the best-fit ellipsoid in the y direction
BA	Burnable absorber
BSE	Backscatter electron
C_{2D}	Minor axis length of the best-fit ellipse
C_{3D}	Minor axis length of the best-fit ellipsoid
$Circ$	Circularity
Rnd	Roundness
$\overline{f}$	Average value of the function $f(z)$
$f(z)$	Function that we seek the average of
FFT	Fast-Fourier transform
FIB	Focused ion beam
HAADF	High-angle annular dark field
HEU	Highly enriched uranium
HIP	Hot isostatic pressing
HPRR	High performance research reactor
HRTEM	High resolution transmission electron microscopy
ID	Identification
LEU	Low-enriched uranium

P	Perimeter
PIE	Post-irradiation examination
R	Radius of the (3D) sphere
r_{SEM}	Radius of the (2D) circular cross-section of a (3D) sphere in an SEM micrograph
RB	Roll bonding
SAED	Selected area electron diffraction
SEM	Scanning electron microscopy
TEM	Transmission electron microscopy
USHPRR	United States High Performance Research Reactor (Program)
V	Lump volume of the BA
$w(z)$	Weight function describing how $f(z)$ is distributed
XEDS	X-ray energy dispersive spectroscopy

1. Introduction

The Advanced Low-Enriched Uranium (aLEU) Program is currently developing power-producing, load-following, long core-life reactor systems with low-enriched (to 19.75%) uranium. Development and licensing of aLEU fuel would be useful for a variety of reactor types that currently use highly enriched uranium (HEU), such as the United States High Performance Research Reactor (USHPRR) Program. The USHPRR is currently pursuing a fuel qualification and licensing effort focused on converting HPRRs in the United States from HEU to high-density low-enriched uranium (LEU) fuel. The fuel in Idaho National Laboratory's Advanced Test Reactor (ATR) currently uses HEU UAl_x fuel with natural B_4C (roughly 20% ^{10}B) embedded in an aluminum-based matrix. The B_4C acts as a burnable neutron absorber (BA) to suppress excess initial reactivity and to help control the power profile. The incorporation of BAs into the LEU fuel under development under the aLEU program would provide benefits similar to that of B_4C in HEU fuel [1, 2].

Experimental studies of metallic burnable absorber plates are scarce in recent years, but they are not without historical precedent. Experiments at the Shippingport reactor in the late 1950s demonstrated the fabrication and irradiation response of zirconium-uranium-boron metallic fuel composed of 90–96 wt% Zircaloy, 3.9–9.9 wt% uranium, and 0.03–0.11 wt% boron [3]. The fueled metallic BA consisted most of the α-zirconium and ε-zirconium-uranium hexagonal phases, but because of its insolubility, the BA was distributed within the fuel matrix as a dispersion of ZrB_2 [3]. These BAs were fabricated by extrusion and hot or cold working of the alloys. The mechanical properties of the zirconium-uranium-boron alloys were found to be strongly affected by variations in both impurity content and fabrication parameters [3]. ZrB_2 is currently used in

commercial nuclear power reactors as a thin-film coating over UO_2 fuel. The helium release from the n,α reaction in ^{10}B diffuses easily through the ZrB_2 matrix, readily resulting in helium release [4]. Other boron-based films have been proposed and fabricated, but details of their performance during use in HPRR conditions are limited [5-7].

Most diboride BA compounds are refractory, inert, stable in aluminum, and have a high melting temperature. They also exhibit better helium retention than their tetraboride and hexaboride counterparts due to their more compact crystal structures in which helium is more effectively trapped [8]. The addition of significant amounts of ceramics to metallic fuel plates can alter their mechanical properties and make plate fabrication more challenging. BA compounds that have a high boron density and less ceramic volume in the foils are therefore preferred. Aluminum boride and zirconium boride can be fabricated in their diboride structures while B_4C is widely available due to its popular use as a BA in both research and commercial nuclear reactors. Applying BAs to the external surface of the AA-6061 cladding were considered as part of this development effort in the form of thin films and rings but were ultimately rejected due to risks and concerns associated with fabricability, hermeticity with the cladding, sputtering, potential galvanic reactions, etc. Consequently, B_4C, aluminum boride, and zirconium boride burnable absorbers embedded within the foil meat were selected for fabrication and testing in the ATR.

Of particular interest in these fabrication and irradiation tests are detrimental phenomena which are exacerbated by the increasing internal gas pressure in the plate as a result of helium buildup from the $^{10}B(n,\alpha)^7Li$ interaction, i.e. fuel swelling and blister anneal failure temperature. The unirradiated unfueled plates were examined in order to establish a baseline on the properties and performance of BA-containing plates. The results of these characterizations will help guide the understanding of plate performance during forthcoming post-irradiation examinations (PIE). Plates containing phases of both BAs and uranium will be discussed in a future manuscript.

This work covers the fabrication and electron microscopy of the BA-containing plates in their unirradiated condition to identify viable methodologies of incorporating the materials into fueled plates. It is critical to document key characteristics, such as porosity and phase identification, of the as-fabricated plates in order to understand irradiation performance, such as porosity and phase identification. Also worth exploring are the size and shape distributions of the BA-containing phases due to the possibility of non-negligible neutron self-shielding effects. Neutron self-shielding occurs when a material that readily absorbs neutrons has physical dimensions which are sufficiently large that the neutron flux within the BA is less than at its surface due to absorption as neutrons travel through it. For BAs containing dense agglomerates of ^{10}B, neutron self-shielding can be noticeable for agglomerates having physical dimensions at length scales on the order of a few microns [9]. Neutron self-shielding reduces the BA burnout rate over the course of the fuel's operational cycle, effectively extending the BA lifetime as compared to a non-shielded BA. In other words, a collection of small BA particles will burn out faster than a single large BA particle of the same total volume. Therefore, this work also investigated both BA size and geometry distributions resulting from these fabrication methods. This information is critical to understand how the BAs would influence reactivity and fuel performance over the course of the fuel's operational cycle.

2. Methods

2.1. Plate Fabrication

The nominal geometries of all BA foils (green) clad in Al-6061 (grey) are identical, as shown in **Figure 1**. The sample identifications (IDs), compositions, forms, and enrichments of the samples discussed in this manuscript are provided in **Table 1**. The ^{10}B concentrations employed in the foils containing B_4C and ZrB_2 are prototypic of what would be employed in LEU plates used in the ATR, while the ^{10}B concentration in the Al-4.5B is much higher but was still investigated for comparison purposes. The increased helium production from the additional ^{10}B in the Al-4.5B foil also offsets the lack of fission gases that would be present in foils containing nuclear fuel.

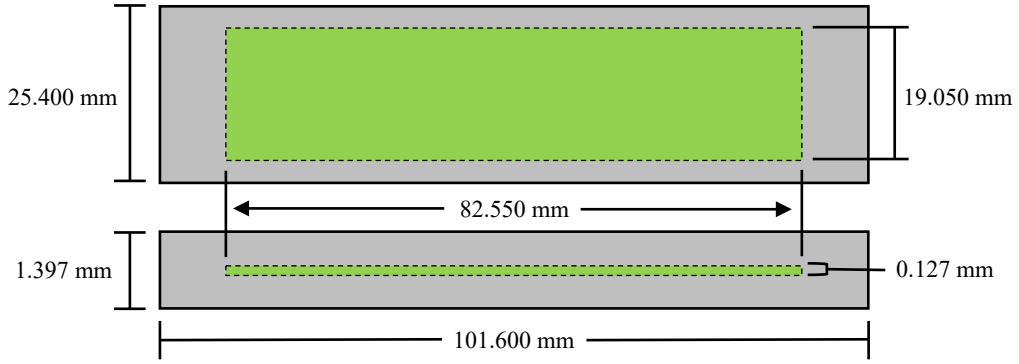

Figure 1: Illustration of the burnable absorber-containing foil (green) clad in Al-6061 (grey), as shown from the front view (top) and side view (bottom, not drawn to scale).

The Al-4.5B foil was fabricated by commercially procuring boron-bearing ingots from Ceradyne, Inc., and then cold rolling them to the desired thickness. The Al-4.5B ingot was commercially manufactured by adding a boron halide to molten aluminum. Next, the foil was sized to the appropriate dimensions (see **Figure 1**) using an existing blank die and hydraulic system. The Al-4.5B foil was then sealed within aluminum alloy AA-6061 cladding via a roll-bonding (RB) process. RB involves heating a prepared rolling assembly in a furnace to 500 ºC for 20 minutes, then passing the assembly multiple times through a rolling mill. The compressive force between the pins was oriented in the vertical (thinnest) direction in **Figure 1** (bottom).

The B_4C and ZrB_2 samples were fabricated by blending 400 mesh (< 37 μm) powders of B_4C and ZrB_2 (supplied by Ceradyne, Inc.) with aluminum powders in an automated Turbula mixer for 2 hours, followed by compacting of the powders, then RB of the material to the desired thickness inside of an aluminum can. The edges of the can were then trimmed, leaving a layer of boron-bearing material sandwiched between two layers of AA-6061 cladding. A second ZrB_2 foil was prepared identically to the previous ZrB_2 sample, with the additional final step of hot isostatic pressing (HIP) to explore the effect of HIP on foil porosity. The only foil that did not experience

HIP shall henceforth be referred to as "ZrB_2-noHIP". HIP of the Al-4.5B, B_4C, and ZrB_2 plates was performed at 560 °C and 103 MPa for 90 minutes with a ramp rate of 280 °C·hr^{-1} as described elsewhere [10].

Table 1: Burnable Absorber Sample Compositions, Forms, and Enrichments

Sample ID	Nominal B Loading (wt%)	^{10}B Enrichment (wt%)	^{10}B Mass in Foil (g)
Al-4.5B	4.5	98.50	0.0235
B_4C	1.9	97.58	0.0079
ZrB_2-noHIP	9.6	75.17	0.0079
ZrB_2	9.6	75.17	0.0079

2.2. Electron Microscopy

Specimens for transmission electron microscopy (TEM) were prepared with a FEI 200 focused ion beam (FIB) microscope using the FIB lift-out technique [11]. TEM was conducted using a FEI Tecnai F30 300 keV TEM equipped with a Fischione high-angle annular dark field (HAADF) detector. Selected area electron diffraction (SAED) was performed to identify the BA-containing phases.

Scanning electron microscopy (SEM) was conducted using a JEOL 7000F FEG SEM and a Zeiss Ultra-55 field emission SEM with X-ray energy dispersive spectroscopy (XEDS). Backscattered electron (BSE) imaging and XEDS were performed on transverse cross sections of the samples (see **Figure 2**) to identify the microstructures and partitioning of the sample constituents amongst different phases.

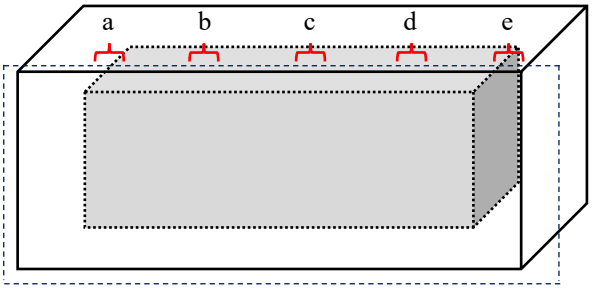

Figure 2: Illustration of the cut (blue dashed line) and transverse cross-section locations of BA-containing foils selected for SEM imaging, where the indicated regions are referred to as (a) left, (b) mid-left, (c) middle, (d) mid-right, and (e) right. The gray region represents the BA-

containing foil which is clad in AA-6061. The SEM electron beam was oriented into the page in this illustration.

2.3. Image Processing

The boron-containing phases in the SEM BSE micrographs are clearly distinguishable based on differences in atomic number contrast with the aluminum-based matrix. The size and shape distributions of the BAs were analyzed on the criteria of cross-sectional area (automatically calculated from the size of the two-dimensional cross section of the particles in pixels and the known size of the scale bar from the raw SEM images), roundness, circularity, and best-fit ellipse aspect ratio (see **Figure 3**) using the ImageJ software developed by the National Institutes of Health. The mathematical definitions of circularity (*Circ*), roundness (*Rnd*), and aspect ratio (*AR*) are defined in **Eq. 1-3**, respectively, where area is in units of μm^2. Circularity is a measure of similarity to a perfect circle, the possible values of which span from zero to one. A circle has a circularity of unity. The closer to zero a feature's circularity is, the less similar it is to a circle. Roundness is similar to circularity as a measure of similarity to a perfect circle; its possible values also span from zero to one, but roundness is insensitive to irregularities associated with the perimeter of the feature (such as a sawtooth-shaped surface, for example), and instead uses the major axis of the feature's best-fit ellipse.

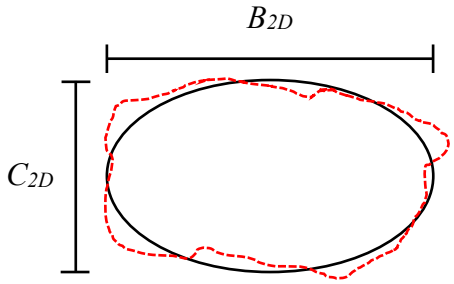

Figure 3: Illustration of the best-fit ellipse (solid black line) overlayed on top of a BA dispersoid (dotted red line).

Eq. 1

$$Circ = 4\pi \frac{A}{P^2}$$

Eq. 2

$$Rnd = \frac{4A}{\pi {B_{2D}}^2}$$

Eq. 3

$$AR = \frac{B_{2D}}{C_{2D}}$$

Where,

Circ = circularity

Rnd = roundness

AR = aspect ratio of the best-fit ellipse

A = area (μm^2)

P = perimeter (μm)

B_{2D} = major axis length of the best-fit ellipse (μm)

C_{2D} = minor axis length of the best-fit ellipse (μm)

3. Results

3.1. Al-4.5B

A montage of SEM micrographs taken at the locations defined in **Figure 2** is shown in **Figure 4** (left) for the Al-4.5B sample. The original micrographs in **Figure 4** (left) were then cropped (**Figure 4**, middle) and converted into black and white (B&W) images shown in **Figure 4** (right). The B&W images were then analyzed for size and shape distributions using ImageJ. Features cut off by the edges of the B&W images were omitted from the analysis as seen in **Figure 4** (middle). As shown in the XEDS spectra in **Figure 5**, the black features are the boron-rich BA phase while the white features are titanium-rich precipitates. TEM SAED patterns of the gray and white particles in the matrix were indexed and identified as AlB_2 (**Figure 6**) and Al_3Ti (**Figure 7**), respectively. The aluminum boride-containing foils were fabricated very close to 100% theoretical density such that errors due to porosity are negligible.

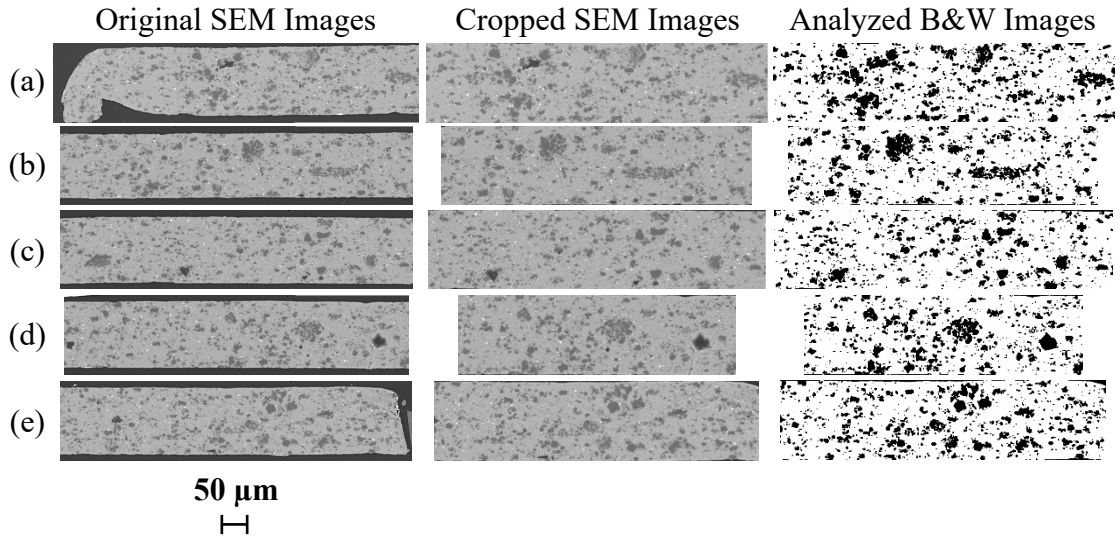

Figure 4: Montage of SEM BSE micrographs from the Al-4.5B sample taken at the (a) left, (b) mid-left, (c) middle, (d) mid-right, and (e) right ends of the foil. The original micrographs are the left column, the cropped SEM images are the middle column, and the cropped micrographs were converted to black and white images in the right column, which were analyzed to determine BA size and shape distribution analysis. Features cut off by the edges of the images were omitted from the analysis. The scale bar is associated with the original SEM images only.

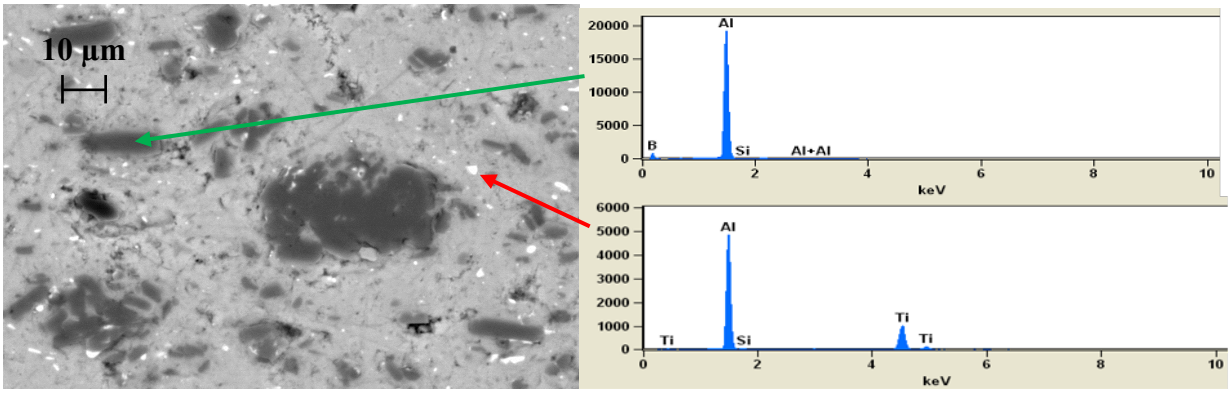

Figure 5: SEM BSE micrograph (left) and XEDS spectra (right) of Al-4.5B sample revealing black features to be boron-rich BA phase in the foil (green arrow) and white particles to be titanium-rich precipitates (red arrow).

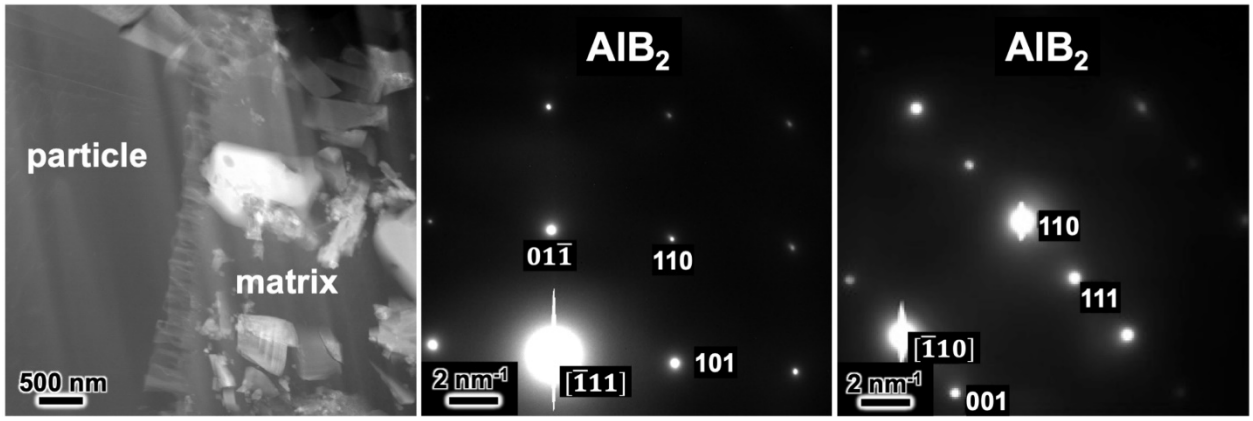

Figure 6: HAADF micrograph of dark particle in the Al-4.5B matrix with its corresponding SAED patterns indexed as AlB_2.

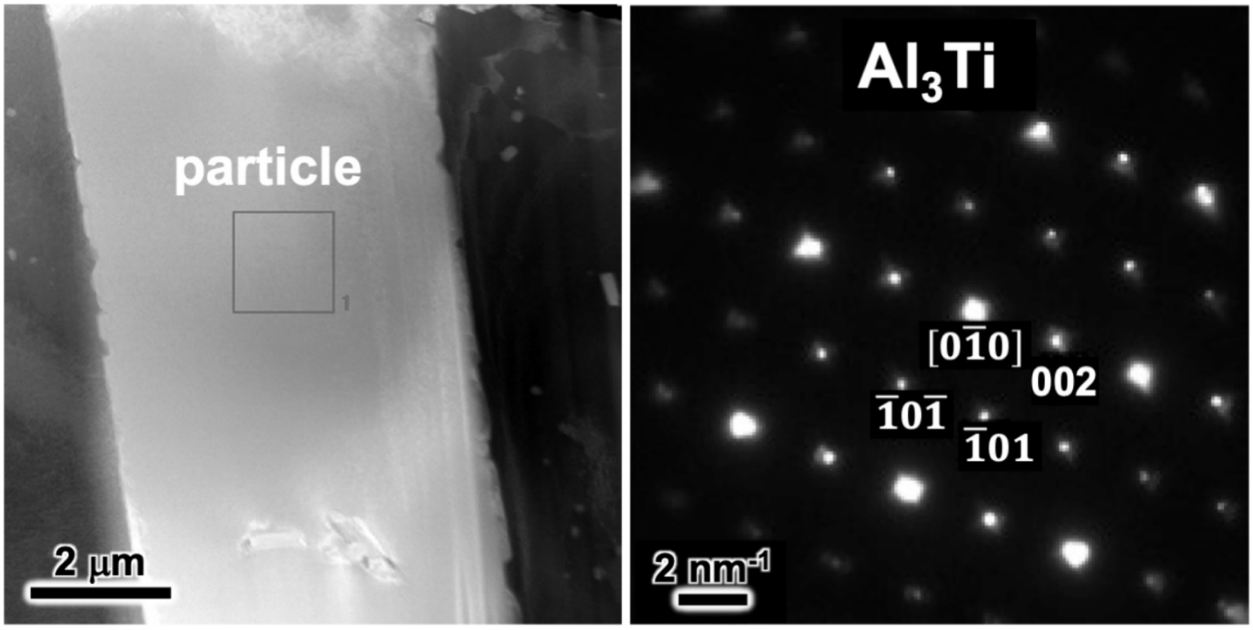

Figure 7: HAADF micrograph of white particle in the Al-4.5B matrix with its corresponding SAED patterns indexed as Al_3Ti.

Figure 8 illustrates the relationship between AlB_2 dispersoid size and aspect ratio. No apparent relationship is found between AR and AlB_2 particle size. Statistically relevant parameters associated with the analysis of the BA phases identified in the Al-4.5B SEM montage are summarized in **Table 2**. The collective data set consisted of 2,766 AlB_2 particles from the Al-4.5B SEM images. Features which were cut off by the edges of the SEM images in **Figure 4** were excluded from the analysis.

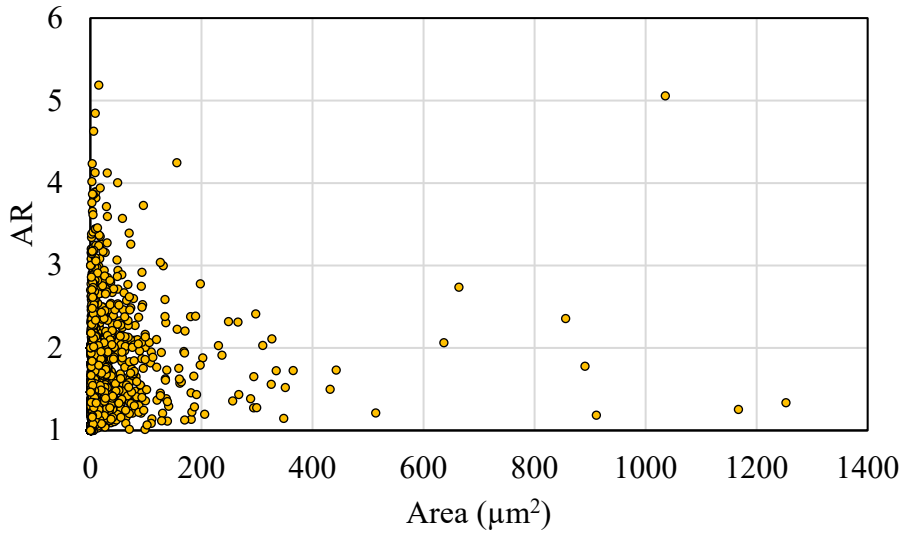

Figure 8: BA aspect ratio vs. area in Al-4.5B revealing that there is no apparent relationship between AR and AlB_2 particle size.

Table 2: Summary of statistical parameters of AlB_2 particles in Al-4.5B. The total data set consisted of 2,766 dispersoids. All dispersoids cut off by the edges of the SEM micrographs were excluded from the analysis.

Parameter	Mean	σ	Min.	Max.
A (μm²)	17.79	62.47	0.164	1252.76
P (μm)	13.54	23.52	1.147	444.09
Circ	0.85	0.20	0.066	1.00
Rnd	0.67	0.18	0.193	1.00
B_{2D} (μm)	4.24	4.82	0.457	81.66
C_{2D} (μm)	2.59	2.67	0.457	34.55
AR	1.62	0.52	1.000	5.19

3.2. B_4C

A montage of SEM BSE micrographs taken at the locations defined in **Figure 2** is shown in **Figure 9** (left) for the foil containing boron carbide. The micrographs in **Figure 9** (left) were cropped (**Figure 9**, middle) and converted into black and white images shown in **Figure 9** (right). The B&W images were used for size and shape analysis in ImageJ. Features cut off by the edges of the B&W images were omitted from the analysis as seen in **Figure 9** (middle). The XEDS spectrum in **Figure 10** indicates that the black features in the micrograph are boron-carbon aggregates of BA material. Also shown in **Figure 10** are Al-Fe-Cr precipitates in the cladding

which are expected to be present in AA-6061 [12]. The boron carbide-containing foils were fabricated very close to 100% theoretical density such that errors due to porosity are negligible.

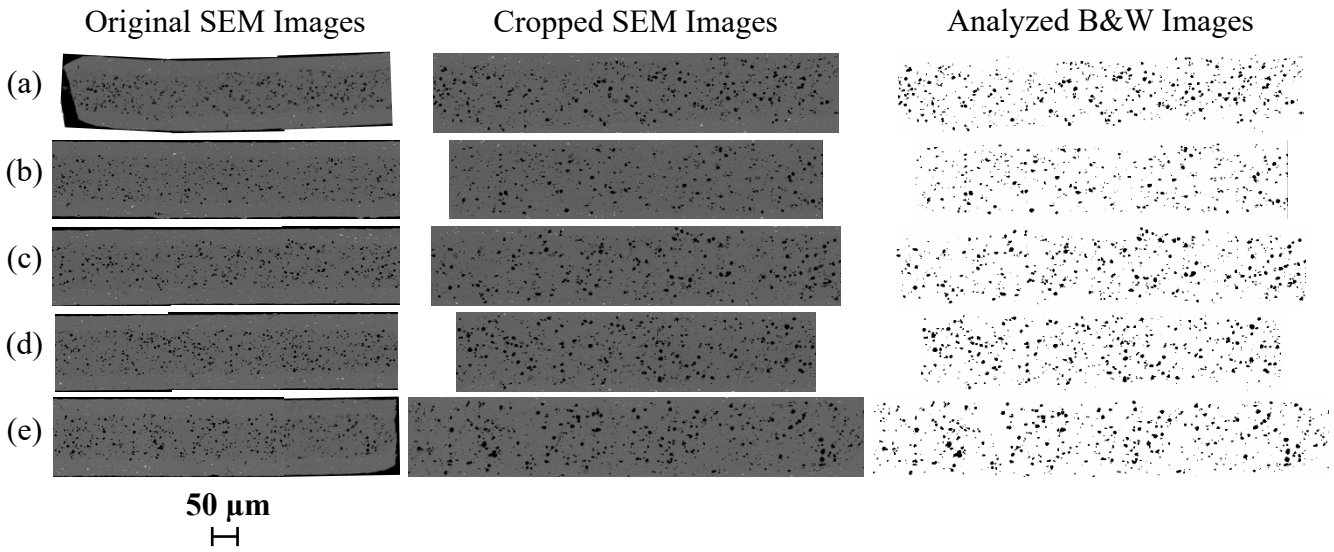

Figure 9: Montage of SEM BSE micrographs from the B_4C sample taken at the (a) left, (b) mid-left, (c) middle, (d) mid-right, and (e) right ends of the foil. The original micrographs images are the left column, the cropped micrographs are the middle column, and the cropped micrographs were converted to B&W images in the right column, which were analyzed to determine BA size and shape distribution analysis. The scale bar is associated with the original SEM images only.

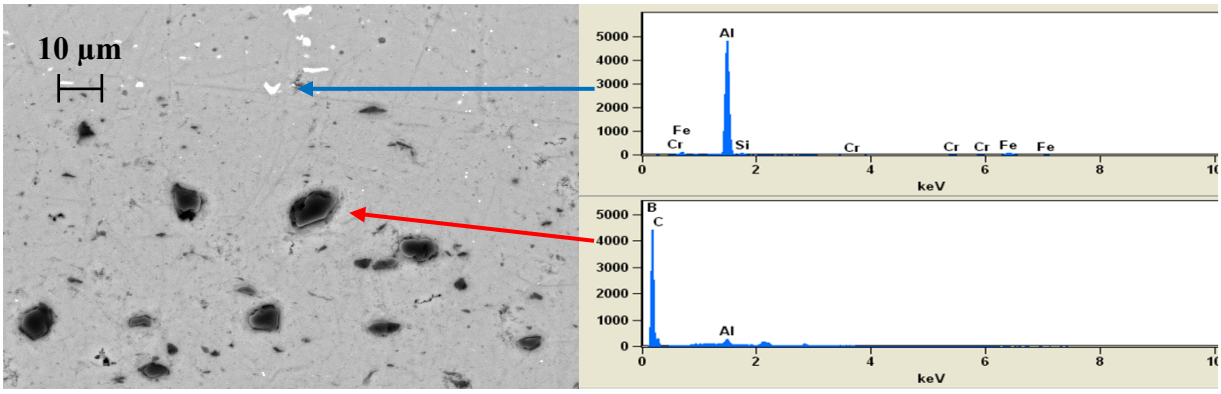

Figure 10: SEM BSE micrograph (left) and XEDS spectra (right) of B_4C sample revealing black features to be boron-carbon rich BA phase in the foil (red arrow) and white particles to be Al-Fe-Cr dispersoids in the AA-6061 cladding (blue arrow).

SAED patterns of the black features in the matrix were indexed and identified as B_4C (**Figure 11**). The decohesion at the interface of the B_4C and the aluminum matrix was observed frequently, as indicated by the red arrows in **Figure 11**, suggesting low wettability/damage between B_4C and the Al matrix. High resolution TEM (HRTEM) micrographs and the corresponding fast-Fourier transformed (FFT) patterns identified the presence of Si at the Al(Si)-B_4C interfaces, shown in **Figure 12**.

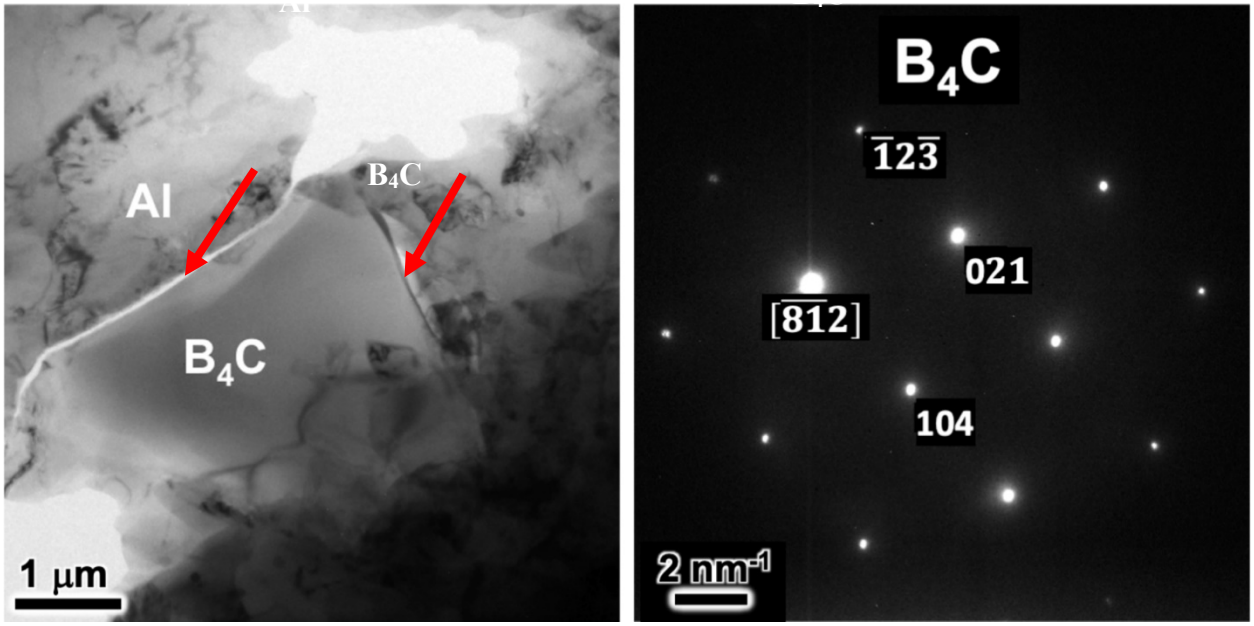

Figure 11: (Left) HAADF micrograph of B_4C particle embedded in aluminum matrix, with debonded interface (red arrows). (Right) SAED pattern confirming the particle to be B_4C.

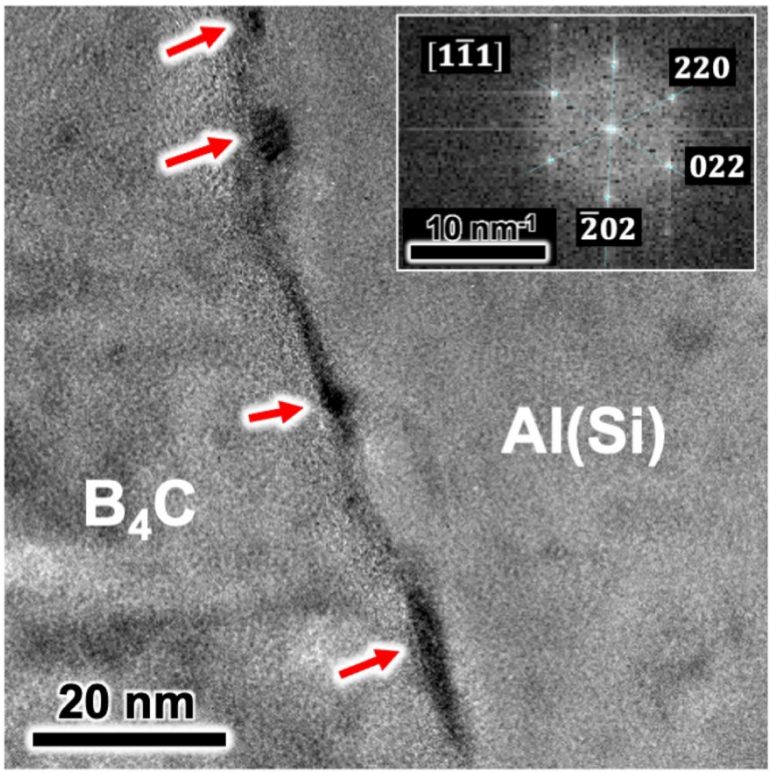

Figure 12: HRTEM micrograph of the dark features at the Al(Si)-B_4C interface (red arrows) with FFT pattern overlayed, indexed as Si.

Figure 13 illustrates the relationship between B_4C dispersoid size and aspect ratio. The smaller B_4C dispersoids appear slightly more elongated than the larger phases. Statistically relevant parameters associated with the analysis of the B_4C particles identified from **Figure 9** are summarized in **Table 3**. The collective data set consisted of 2,496 B_4C particles embedded in the Al matrix. Particles which were cut off by the edges in **Figure 9** (middle) were excluded from the analysis.

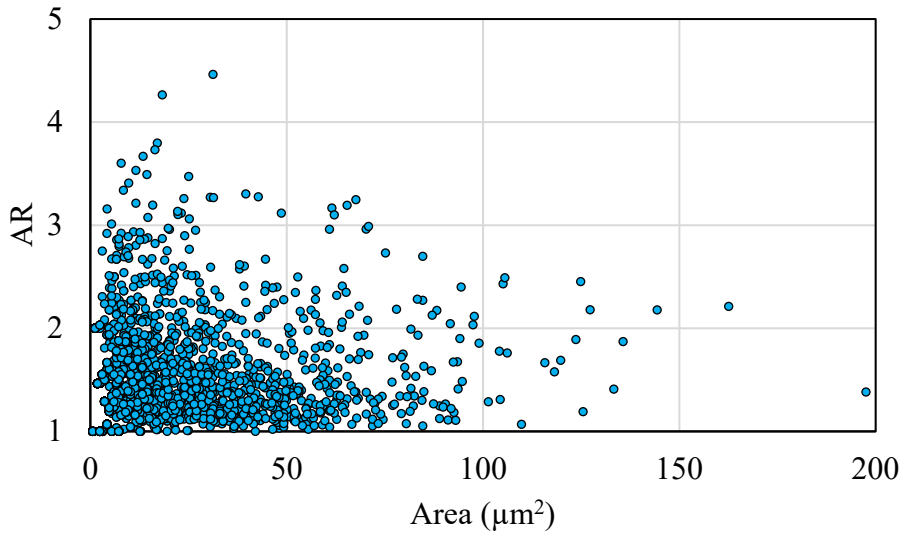

Figure 13: BA aspect ratio vs. area in B_4C embedded in Al revealing that the smaller dispersoids tend to be more elongated than the larger dispersoids.

Table 3: Summary of statistical parameters of B_4C particles embedded in Al. The total data set consisted of 2,496 dispersoids. All dispersoids cut off by the edges of the SEM BSE micrographs were excluded from the analysis.

Parameter	Mean	σ	Min.	Max.
A (μm²)	17.41	21.54	0.60	197.51
P (μm)	13.33	9.85	2.19	94.56
Circ	0.92	0.13	0.23	1.00
Rnd	0.70	0.18	0.22	1.00
B_{2D} (μm)	4.90	3.25	0.87	21.40
C_{2D} (μm)	3.30	2.09	0.87	13.49
AR	1.53	0.46	1.00	4.46

3.3. ZrB_2-noHIP

A montage of SEM BSE micrographs taken at the locations defined in **Figure 2** is shown in **Figure 13 Figure 14** (left) for the ZrB_2-noHIP sample. The micrographs in **Figure 14** (left) were cropped (**Figure 14**, middle) and converted into black and white images shown in **Figure 14** (right). The B&W images were used for size and shape analysis in ImageJ. Features cut off by the edges of the B&W images were omitted from the analysis. As shown in the micrographs, the ZrB_2-noHIP foil had large regions of porosity. The porosity in these samples did not impact

quantitative imaging analysis, however, because they were easy to discriminate based on contrast (black) from the BA phases (white). The XEDS spectrum in **Figure 15** confirms that the white features in the SEM BSE micrographs are boron-zirconium aggregates, while the dark features are Al-Mg-Si precipitates. Visual examination of **Figure 14** indicates that the BA phases in this material are much smaller in size than in the Al-4.5B or B_4C samples.

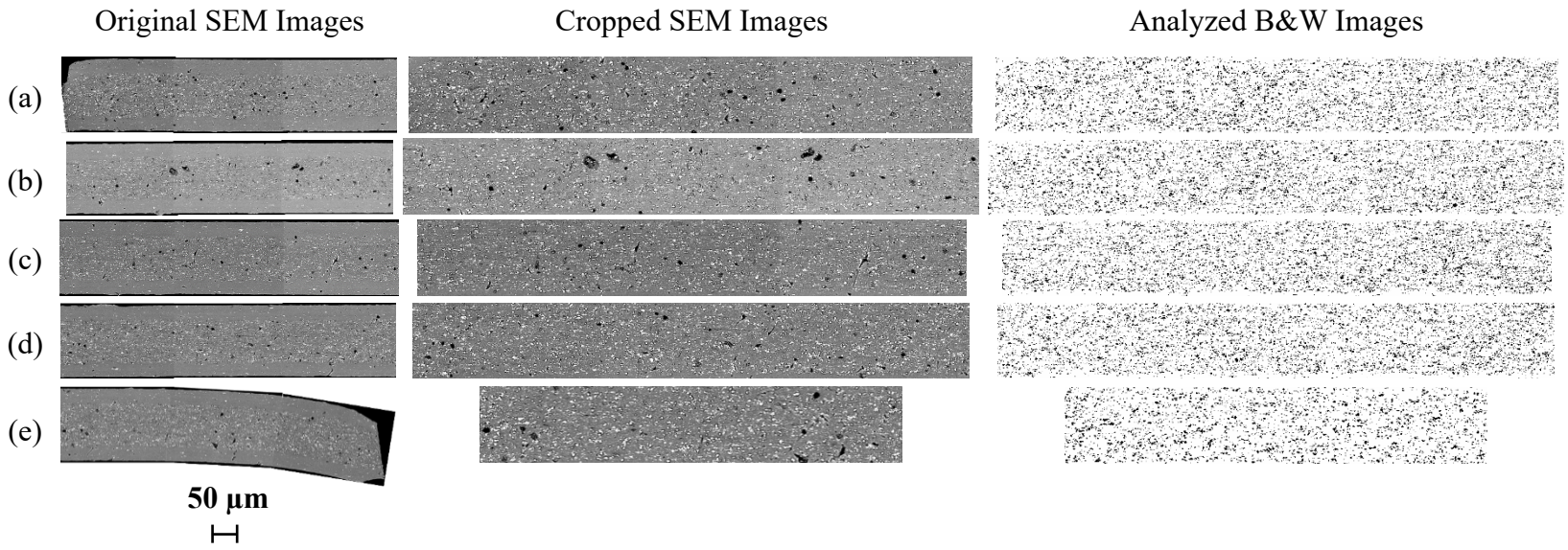

Figure 14: Montage of SEM BSE micrographs from the ZrB_2-noHIP sample taken at the (a) left, (b) mid-left, (c) middle, (d) mid-right, and (e) right ends of the foil. The original micrographs are the left column, the cropped micrographs are the middle column, which were converted into the black and white images in the right column which were analyzed to determine BA size and shape distribution analysis. Features cut off by the edges of the images were omitted from the analysis. The scale bar is associated with the original SEM images only.

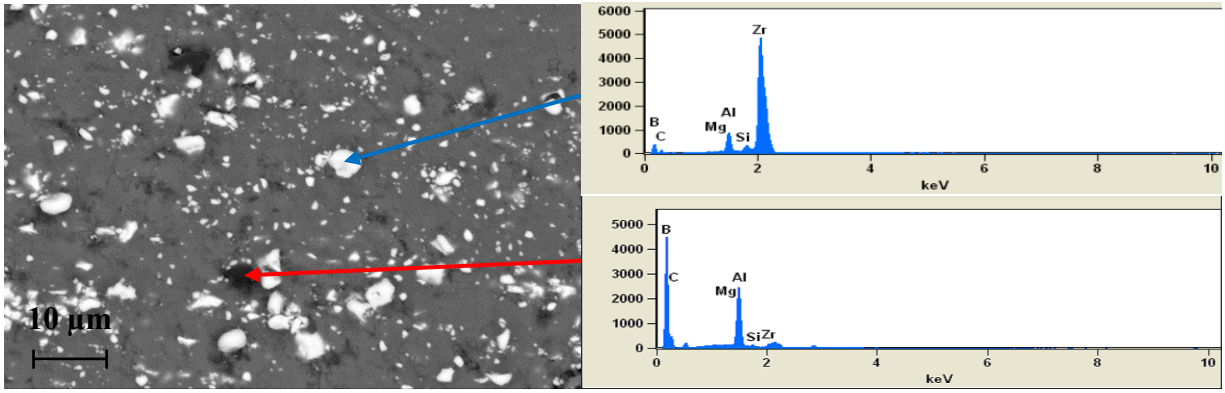

Figure 15: SEM BSE micrograph (left) and XEDS spectra (right) of ZrB_2-noHIP sample revealing white features to be boron-zirconium rich BA phase in the foil (blue arrow) and black features to be Al-Mg-Si precipitates in the foil matrix (red arrow).

FFT diffraction patterns from the HRTEM (**Figure 14**) were indexed and identified as ZrB_2. The cohesion at the interface of the ZrB_2 and the surrounding aluminum matrix appears to be sharper and more continuous than for the B_4C, as indicated by the red arrow in **Figure 16**.

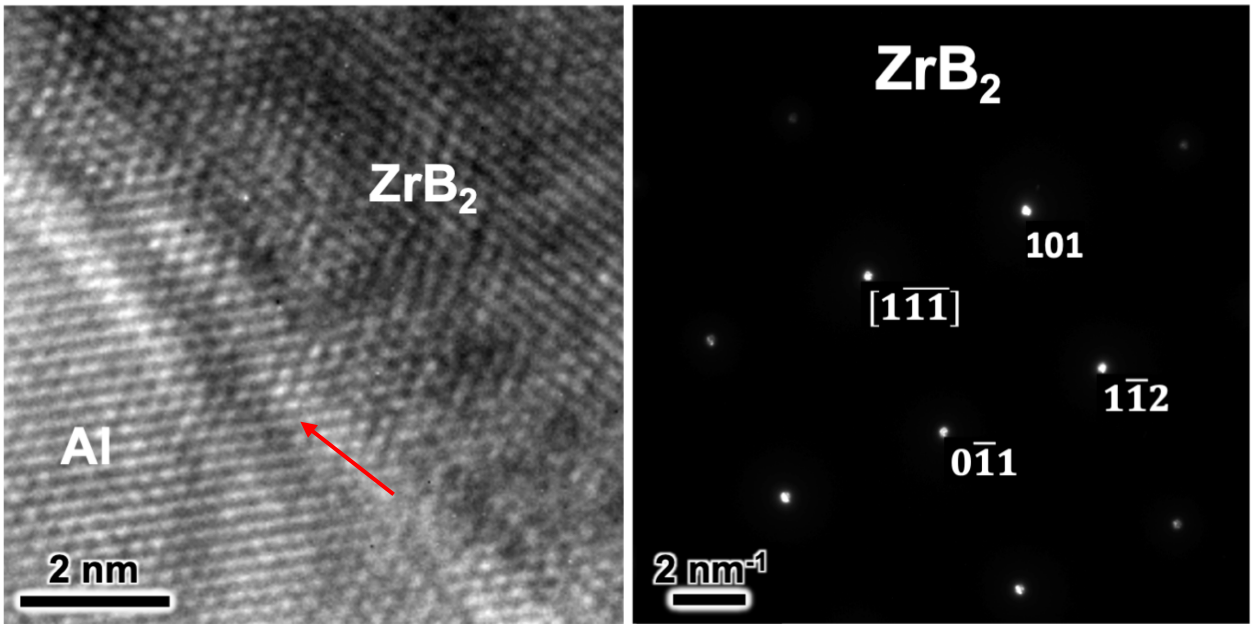

Figure 16: (Left) HRTEM micrograph of a ZrB_2 particle in the non-HIP'd foil embedded in the aluminum matrix, with strong bonding at the interface (red arrows). (Right) FFT diffraction pattern confirming the particle to be ZrB_2.

Figure 17 illustrates the relationship between ZrB_2-noHIP dispersoid size and aspect ratio. While the ZrB_2-noHIP BA particles appear more elongated than the AlB_2 or B_4C particles, the ZrB_2-noHIP BA phases are also smaller in size. Statistically relevant parameters associated with the analysis of the ZrB_2-noHIP BA particles identified from **Figure 14** are summarized in **Table 4**. The collective data set consisted of 28,684 dispersoids. Particles which were cut off by the edges of the SEM images in **Figure 14** were excluded from the analysis.

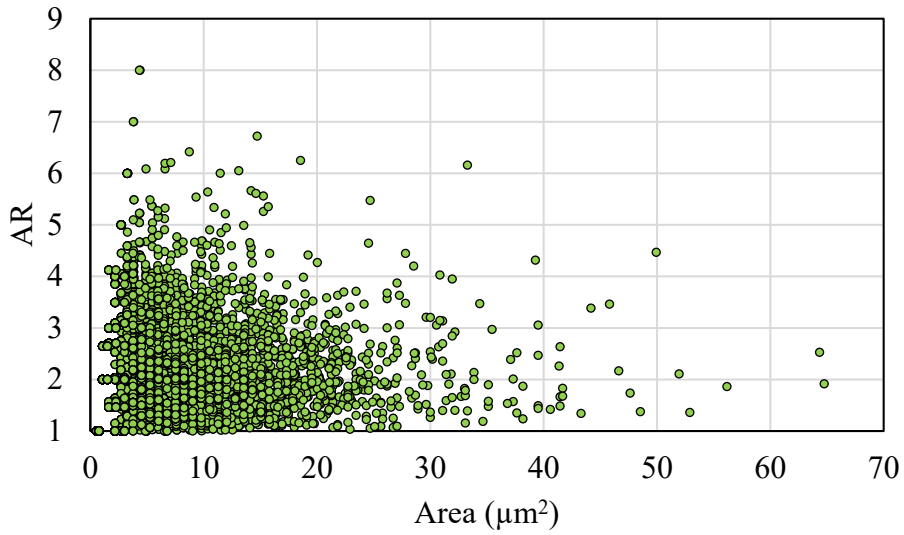

Figure 17: BA aspect ratio vs. area in ZrB_2-noHIP revealing that these BA particles are more elongated and smaller than those found in the Al-4.5B or B_4C samples.

Table 4: Summary of statistical parameters of ZrB_2-noHIP BA particles. The total data set consisted of 28,684 dispersoids. All particles cut off by the edges of the SEM micrographs were excluded from the analysis.

Parameter	Mean	σ	Min.	Max.
A (μm²)	2.81	3.98	0.54	64.75
P (μm)	5.50	4.97	2.08	74.98
Circ	0.91	0.17	0.12	1.00
Rnd	0.70	0.25	0.13	1.00
B_{2D} (μm)	2.16	1.53	0.83	16.85
C_{2D} (μm)	1.27	0.68	0.71	7.03
AR	1.65	0.71	1.00	8.00

3.4. ZrB_2

The ZrB_2 images discussed in the previous section revealed many regions of porosity. The plate discussed in this section is identical to the plate from the previous section with the additional step of HIP. A montage of SEM BSE micrographs taken at the locations defined in **Figure 2** is shown in **Figure 18** (left) for the ZrB_2 sample. The micrographs in **Figure 18** (left) were cropped (**Figure 18**, middle) and converted into B&W images shown in **Figure 18** (right). The B&W images were used for size and shape analysis in ImageJ. Features cut off by the edges of the B&W images were omitted from the analysis. As shown by the BSE micrographs, the ZrB_2 contains fewer regions of porosity, suggesting that the HIP process reduces the voids shown in **Figure 14**. The porosity (black features in **Figure 17**) is easily distinguishable in ImageJ from the BA regions (white) based on contrast and was not included the forthcoming analysis. The XEDS spectrum in **Figure 19** confirms that the white features in the BSE micrographs are boron-zirconium aggregates of BA material (remaining unchanged from before HIP). Visual examination of **Figure 18** indicates that the BA phases in this material remain much smaller in size than in the Al-4.5B or B_4C samples after the HIP process.

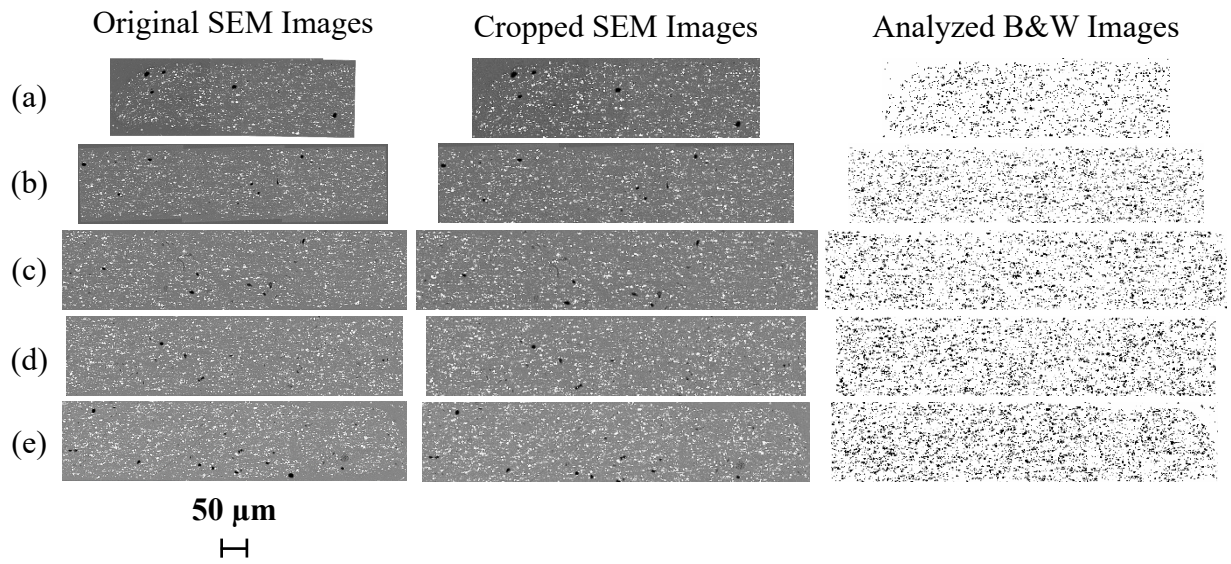

Figure 18: Montage of SEM BSE micrographs from the ZrB_2 sample taken at the (a) left, (b) mid-left, (c) middle, (d) mid-right, and (e) right ends of the foil. The original micrographs are the left column, the cropped micrographs are the middle column, which were converted into the black and white images in the right column which were analyzed to determine BA size and shape distribution analysis. Features cut off by the edges of the images were omitted from the analysis. The scale bar is associated with the original SEM images only.

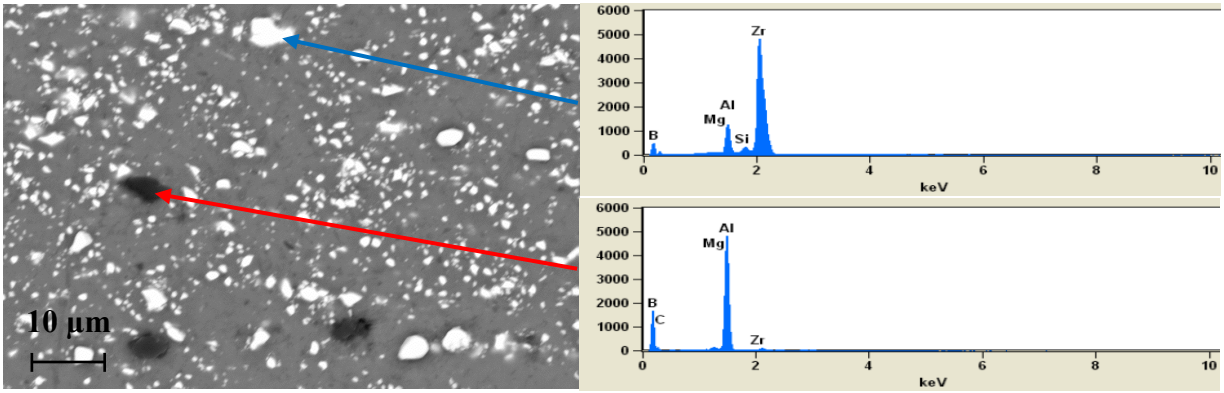

Figure 19: SEM BSE micrograph (left) and XEDS spectra (right) of ZrB_2 sample revealing white features to be boron-zirconium rich BA phase in the foil (blue arrow) and black features to be Al-Mg precipitates in the foil matrix (red arrow).

Figure 20 illustrates the relationship between ZrB_2 dispersoid size and aspect ratio. After HIP, the particles appear to remain more elongated than the AlB_2 or B_4C particles and are still smaller in size. Statistically relevant parameters associated with the analysis of the ZrB_2 particles identified in **Figure 18** are summarized in **Table 5**. The collective data set consisted of 23,413 ZrB_2 particles embedded in the Al matrix. Particles which were cut off by the edges of the SEM micrographs in **Figure 18** were excluded from the analysis.

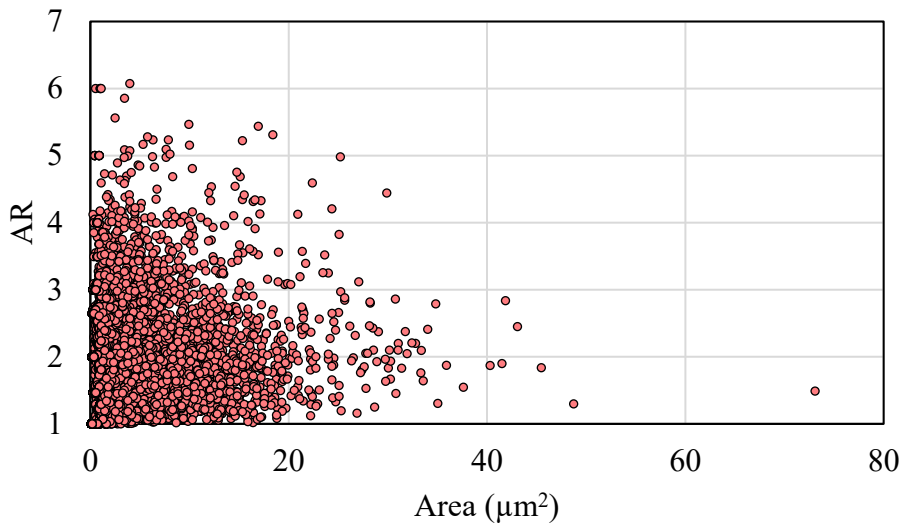

Figure 20: BA aspect ratio vs. area in ZrB_2 embedded in Al revealing that the particles remain more elongated and smaller than those found in the Al-4.5B or B_4C samples after HIP.

Table 5: Summary of statistical parameters of ZrB_2 particles embedded in Al. The total data set consisted of 23,413 dispersoids. All particles cut off by the edges of the SEM images were excluded from the analysis.

Parameter	Mean	σ	Min.	Max.
A (μm^2)	1.90	3.39	0.088	73.077
P (μm)	4.31	4.57	0.841	77.252
Circ	0.90	0.17	0.141	1.000
Rnd	0.69	0.23	0.165	1.000
B_{2D} (μm)	1.62	1.39	0.336	13.002
C_{2D} (μm)	0.96	0.70	0.286	7.905
AR	1.64	0.62	1.000	6.074

4. Discussion

The aluminum boride and zirconium boride foils crystallized in their diboride forms, indicating that they will be more effective at trapping helium than in their tetraboride or hexaboride counterparts due to the more compact diboride crystal structures [8]. Incomplete cohesion between the B_4C dispersoids and the matrix was observed in TEM micrographs (see **Figure 11**). This suggests a debonded interface between the B_4C and the underlying aluminum matrix [13]. From a radiation performance perspective, debonded interfaces and porosity should have a higher affinity toward helium accumulation (which is released from ^{10}B following neutron absorption) than well-bonded pore-free materials, such as those found in the other foils investigated in this study. Further, because of the incomplete bonding at incoherent interfaces, the B_4C precipitates offer little to no resistance to deformations of the surrounding matrix [13]. The linear thermal expansion coefficients of AA-6061 and B_4C are approximately $23 \cdot 10^{-6}$ K^{-1} and $6 \cdot 10^{-6}$ K^{-1}, respectively. This difference in thermal expansion between the particles and the matrix could cause debonding at the interface as the foils are heated or cooled during fabrication. Second, interatomic bonding in B_4C is dominated by covalent forces, while the bonds in the aluminum matrix are metallic in nature [14]. This difference in bonding character between the ceramic and metallic materials may inherently prevent well-adhered interfaces from forming. The cause of the poor interface between these materials warrants further study.

The ZrB_2-noHIP particles had an average dispersoid area of 2.81 ± 3.98 μm^2 as determined by analyzing cross-sectional samples. HRTEM revealed that the bonding at the interface of the ZrB_2-noHIP and the surrounding aluminum matrix appears to be more consistent than for the B_4C. XEDS identified the presence of Al-Mg-Si contaminants within the foil matrix. SEM BSE micrographs also revealed regions of porosity in the foil containing ZrB_2 prior to HIP. The porosity decreased after HIP while the ZrB_2 phase remained unchanged. This is to be expected from the HIP process as compaction occurs through diffusion bonding, creep, and plastic deformation [15, 16]. However, the average dispersoid area of ZrB_2 particles decreased to 1.90 ± 3.39 μm^2 after HIP. It is unlikely that the physical dimensions of the ZrB_2 particles changed during HIP, for which the peak temperature was 560 °C; ZrB_2 is a high temperature material whose

melting temperature is about 3000 °C (compared to a melting temperature of about 585 °C for AA-6061), and microscopy revealed no evidence of interactions between the two materials following HIP. It is likely that the rolling process preferentially oriented elongated ZrB_2 particles within the foil, making the particles appear larger prior to HIP. This preferential orientation could have been reduced during HIP as the AA-6061 matrix evolved and densified around it. This has not been confirmed and warrants further study.

The burnout rates of the BAs inherently depend on the neutron energy spectrum of the reactor in which they will be used. The size and shape distributions of the BAs also influence their burnout rates due to neutron self-shielding, but the information obtained from electron microscopy is only two-dimensional. We therefore consider the approximations that the particles observed in two-dimensional (2D) cross-sectional micrographs, on average, are either (a) three-dimensional (3D) spheres or (b) 3D ellipsoids. A true 3D description of the BA particles would be more accurate and could be more accurately determined by analyzing cross-sectional SEM micrographs taken from different orientations or determined directly using advanced 3D characterization techniques like micro-computed tomography [17].

An illustration of the 2D cross-section of circles which appear from randomly distributed 3D spheres is presented in **Figure 21** (top). Note that even if all the spheres within the matrix are the same size, the circular cross sections which appear in micrographs have different radii due to the random depth at which the cross-section cuts through the sphere. The radii of circles in a 2D image are henceforth defined as r_{SEM} (**Figure 21**, bottom left), and the radii of the 3D sphere is defined as R (**Figure 21**, bottom right). Using the coordinate system defined in **Figure 21**, the spheres are centered at $(0,0,R)$ and are defined in Cartesian coordinates by **Eq. 4**.

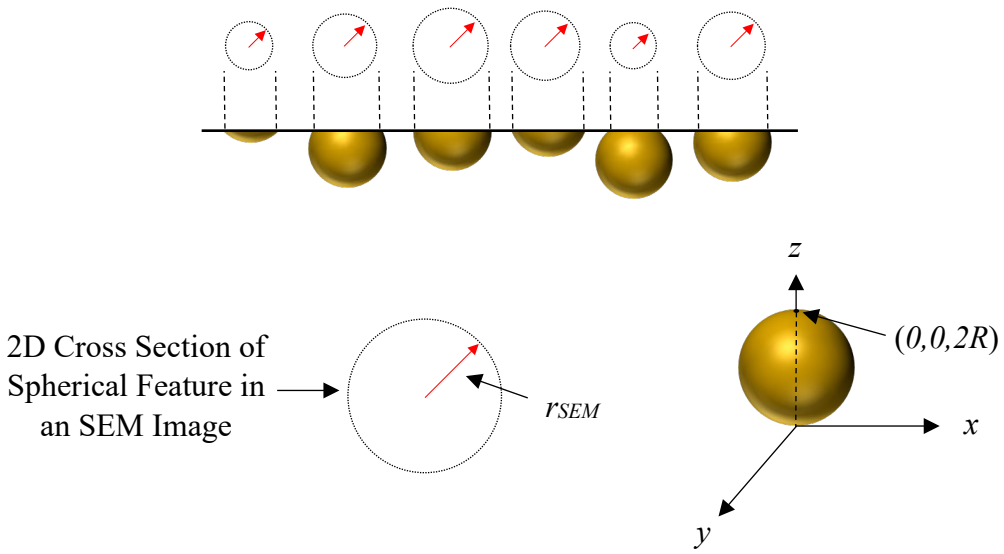

Figure 21: Illustration of the cross-sectional image of circles of radii r_{SEM} which would appear in SEM micrographs resulting from randomly distributed spheres of radius R embedded within the sample matrix.

Eq. 4

$$r_{SEM}^2 + \left(z - R\right)^2 = R^2$$

The average value of a function *f* which is distributed via a weight function *w* may be determined using **Eq. 5**. In this derivation, we seek to define a relationship between r_{SEM} and *R* where the weight function is unity due to the assumption that the particles are embedded randomly about the thickness of the matrix. Combining **Eq. 4** and **Eq. 5**, integrating from *0* to *2R* and rearranging yields the true 3D radius *R* as a function of r_{SEM} in **Eq. 6** according to the spherical dispersoid model. This calculated value *R* is about 1.273 times larger than r_{SEM}, meaning that the average 3D radius of the spherical particles is 1.273 times larger than the circles' radii viewed in 2D cross-sectional images. The volume of the spherical BA dispersoids can then be calculated via **Eq. 7**. Because volume scales with radius to the third power, the difference in calculated volume when using r_{SEM} vs. *R* in **Eq. 7** is more than a factor of two.

Eq. 5

$$\overline{f} = \frac{\int_{\min}^{\max} f(z) \cdot w(z) dz}{\int_{\min}^{\max} w(z) dz}$$

Where,

$\overline{f}$ = average value of the function $f(z)$

$f(z)$ = function that we seek the average of

$w(z)$ = weight function describing how $f(z)$ is distributed

$$\overline{r}_{SEM} = \frac{\int_0^{2R} \left(\sqrt{R^2 - \left(z - R\right)^2}\right) dz}{\int_0^{2R} 1 dz} = \frac{\pi R}{4}$$

Eq. 6

$$R = \frac{4\overline{r}_{SEM}}{\pi}$$

Where

R = 3D radius of the BA via the spherical model

$r_{SEM} = \sqrt{\frac{A}{\pi}}$ = 2D cross-sectional radius of the BA shown in SEM images via the spherical model

A = area of the BA (determined directly from image processing)

Eq. 7

$$V_{sph} = \frac{4}{3}\pi R^3$$

Where

V_{sph} = volume of a spherical BA

Image orientation analysis shows that the average BA dispersoid is not spherical. Visual inspection of the SEM micrographs (**Figure 4**, **Figure 9**, **Figure 14**, and **Figure 18**) suggests that the elongated BA dispersoids are preferentially oriented with the minor axis of their fitted ellipses parallel to the thinnest dimension of the plates. Such a preferential orientation is to be expected due to vertically compressive forces from rolling. Since 3D microscopy was not performed on the as-fabricated plates, we consider the possibility that the average BA dispersoid is an oblate ellipsoid orientated with its minor axis parallel to the *z* direction and its major axes orientated parallel to the *x*-*y* plane according to **Figure 22**. The *x*-*y* plane in **Figure 22** is parallel to the length and width (the longer dimensions, see **Figure 1**) of the plates.

Using these assumptions and orientation parameters shown in **Figure 22**, the average 3D volume of the oblate ellipsoids can be calculated from the 2D elliptical cross sections by using **Eq. 5** where the function *f* represents the area of the 2D elliptical cross sections (on the *y*-*z* plane) viewed in SEM micrographs written in terms of the depth (in the *x* direction) at which the samples were prepared, shown in **Eq. 8**. The assumption that the depth in the dispersoids that the cuts were made is random yields a weight function of unity.

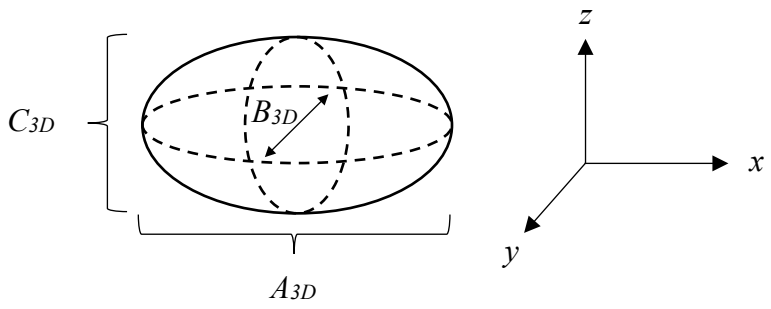

Figure 22: Illustration of the average BA dispersoid which is assumed to be an oblate ellipsoid where $A_{3D} = B_{3D} > C_{3D}$. The *y*-*z* plane represents the cross-sectional surface shown in SEM images.

Eq. 8

$$\overline{f} = \frac{2 \cdot \int_0^{A_{3D}/2} \pi x \cdot \frac{x}{AR} dx}{\int_0^{A_{3D}/2} 1 dx}$$

where

$\overline{f}$ = Average elliptical 2D cross-sectional area as a function of depth x

$\pi x \cdot \frac{x}{AR}$ = Area of the elliptical 2D cross section as a function of depth x

$\therefore$

$$\overline{f} = \frac{\pi}{6AR} A_{3D}^2$$

Eq. 8 relates the average cross-sectional area of elliptical BA features measured from 2D SEM cross-sectional micrographs to their 3D major axis A_{3D} where $A_{3D} = B_{3D}$ and the minor axis C_{3D} is parallel to the z direction. The minor axis is defined by the aspect ratio in **Eq. 3**. This allows the calculation of the average volume of oblate elliptical BA dispersoids using **Eq. 9**.

Eq. 9

$$V_{ell} = \frac{\pi}{6} A_{3D}^2 C_{3D}$$

Where

V_{ell} = volume of an oblate elliptical BA whose minor axis is parallel to the z axis (see **Figure 22**)

$$A_{3D} = \sqrt{\frac{3}{2} AR \cdot B_{2D} C_{2D}}$$

$$C_{3D} = \frac{A_{3D}}{AR}$$

The average volumes of the BA dispersoids investigated in this study according to the spherical (**Eq. 7**) and ellipsoidal (**Eq. 9**) models are summarized in **Table 6**. The ellipsoidal model consistently predicts the average volume of the BA dispersoids to be notably larger (between 20% and 100%) than the spherical model. This discrepancy between the volumes and shapes of the BA dispersoids could impact BA burnout rates due to differences in neutron self-shielding.

Table 6: BA dispersoid volumes calculated from 2D cross-sectional imaging analysis using the spherical and ellipsoidal models, where σ is standard deviation.

Material	Geometric Model	Avg. Vol. (μm^3)	σ (μm^3)
Al-4.5B	Spherical	336	2678
	Ellipsoidal	405	3394
B_4C	Spherical	167	312
	Ellipsoidal	209	508
ZrB_2-noHIP	Spherical	11	29
	Ellipsoidal	23	110
ZrB_2	Spherical	5	15
	Ellipsoidal	7	27

5. Conclusions

In this paper, several BA candidates have been embedded in aluminum matrices, fabricated into foils, and clad in AA-6061 to determine their characteristics prior to irradiation as aLEU fuel plates. Three different materials were examined: boron carbide, aluminum boride, and zirconium boride. The ^{10}B in the BAs had enrichments of 98.5%, 97.58%, and 75.17%, respectively. The BA-containing phases within the foils were characterized using TEM with SAED and SEM with XEDS. The main objective of these characterizations was to establish baseline BA-containing plate properties in order to guide the understanding of plate performance and observations from

forthcoming PIE. The microstructural phases, physical distributions within the plates, bonding with the matrix, and size and shape distributions of the BA phases has been established. The aluminum and zirconium boride BAs crystallized in their diboride structures, which tend to have better helium retention than their tetraboride and hexaboride counterparts due to their more compact crystal structures in which helium is more effectively trapped [8]. The BA-containing phases were mostly homogeneous, indicating that the relatively homogeneous helium release from the $^{10}B(n,\alpha)^{7}Li$ reaction should result in homogeneous swelling and smaller drop in blister anneal temperature from irradiation.

The size and shape distributions of the BA-containing phases were analyzed based on the SEM micrographs using ImageJ. The AlB_2 particles had an average dispersoid area of 17.79 ± 62.47 μm^2, as determined by analyzing SEM cross-sectional micrographs. Phases of contaminated species, particularly Al_3Ti, were frequently observed within the foil matrix from the low-purity powders that were used as feedstock by the commercial vendor using HRTEM diffraction analysis.

TEM SAED patterns showed that the BA-containing phases in the foils containing B_4C embedded in aluminum remained B_4C after cladding in AA-6061. The B_4C particles had an average dispersoid area of 17.41 ± 21.54 μm^2 as determined by analyzing cross-sectional samples. HRTEM revealed incomplete cohesion at the interface of the B_4C and the aluminum matrix. Such debonded interfaces generally offer little to no resistance to deformations of the surrounding matrix. These interfaces are also expected to be more sensitive to helium accumulation HRTEM analysis identified the presence of Si contamination at the Al(Si)-B_4C interfaces. Several possible causes of the poor bonding at the B_4C-6061 interface have been identified.

The ZrB_2-noHIP particles had an average dispersoid area of 2.81 ± 3.98 μm^2 as determined by analyzing cross-sectional samples. HRTEM revealed that the bonding at the interface of the ZrB_2-noHIP and the surrounding aluminum matrix appears to be more consistent than for the B_4C. SEM BSE micrographs also revealed regions of porosity in the foil containing ZrB_2 prior to HIP. The porosity decreased after HIP while the ZrB_2 phase remained unchanged. However, the average dispersoid area of ZrB_2 particles decreased to 1.90 ± 3.39 μm^2 after HIP. This is likely due to preferential orientation of ZrB_2 particles due to the rolling process which could have been more randomly reoriented during HIP as the AA-6061 matrix evolved and densified around it. This has not been confirmed and warrants further study.

A method of approximating the true 3D volume of the dispersoids observed in 2D cross-sectional micrographs is presented using both spherical and ellipsoidal models. The average volume of dispersoids calculated using the ellipsoidal model is much larger (20–100%) than the spherical model; this could influence BA burnout rates due to differences in neutron self-shielding effects, as determined by forthcoming neutronics simulations.

Acknowledgements

This manuscript has been authored by Battelle Energy Alliance, LLC, under Contract No. DEAC07- 05ID14517 with the U.S. Department of Energy. The United States Government retains

and the publisher, by accepting the article for publication, acknowledges that the United States Government retains a nonexclusive, royalty-free, paid-up, irrevocable, world-wide license to publish or reproduce the published form of this manuscript, or allow others to do so, for United States Government purposes. The authors declare that they have no known competing financial interests or personal relationships that could have appeared to influence the work reported in this paper.

References

[1] J. Gan, B.D. Miller, D.D. Keiser, J.F. Jue, J.W. Madden, A.B. Robinson, H. Ozaltun, G. Moore, M.K. Meyer, Irradiated Microstructure of U-10mo Monolithic Fuel Plate at Very High Fission Density, J Nucl Mater 492 (2017) 195-203.
[2] D. Keiser, J.F. Jue, B. Miller, J. Gan, A. Robinson, J. Madden, Observed Changes in as-Fabricated U-10mo Monolithic Fuel Microstructures after Irradiation in the Advanced Test Reactor, Jom-Us 69(12) (2017) 2538-2545.
[3] W.K. Anderson, Neutron Absorber Materials for Reactor Control, Naval Reactors, Division of Reactor Development, U.S. Atomic Energy Commission, Washington, 1962.
[4] S.C. Middleburgh, D.C. Parfitt, P.R. Blair, R.W. Grimes, Atomic Scale Modeling of Point Defects in Zirconium Diboride, J Am Ceram Soc 94(7) (2011) 2225-2229.
[5] J. Musil, R. Cerstvy, A. Pogrebnjak, Thermal Stability of Hard Tantalum Boride Films, High Temp Mater P-Us 24(3) (2020) 193-200.
[6] V. Buranich, A. Pogrebnjak, P. Budzynski, I. Shelest, A. Proszynski, D. Chocyk, A. Goncharov, A. Yunda, Mechanical and Tribological Characterization of Nanostructured Hfb2 Films Deposited from Compound Target, Sn Appl Sci 2(4) (2020).
[7] D.E. Wiley, W.R. Manning, O. Hunter, Elastic Properties of Polycrystalline Tib2 Zrb2 and Hfb2 from Room Temperature to 1300 Degrees K, J Less-Common Met 18(2) (1969) 149-&.
[8] G.W. Gibson, M.J. Graber, Et.Al., Preliminary Report on the Development of Boron Aluminum Foils as Controllable Neutron Absorbers in Aluminum-Clad Nuclear Reactor Fuel Elements, Idaho Nuclear Corporation Report Ci-L 090, 1968.
[9] V.S. Volkov, A.S. Luk'yanov, V.V. Chapkunov, V.P. Shevyakov, V.S. Yamnikov, Use of Burnable Poisons in Nuclear Reactors, The Soviet Journal of Atomic Energy 11(2) (1962) 745-757.
[10] J.F. Jue, B.H. Park, C.R. Clark, G.A. Moore, D.D. Keiser, Fabrication of Monolithic Rertr Fuels by Hot Isostatic Pressing, Nucl Technol 172(2) (2010) 204-210.
[11] L.A. Giannuzzi, J.L. Drown, S.R. Brown, R.B. Irwin, F. Stevie, Applications of the Fib Lift-out Technique for Tem Specimen Preparation, Microsc Res Techniq 41(4) (1998) 285-290.
[12] M. Hakem, S. Lebaili, S. Mathieu, D. Miroud, A. Lebaili, B. Cheniti, Effect of Microstructure and Precipitation Phenomena on the Mechanical Behavior of Aa6061-T6 Aluminum Alloy Weld, Int J Adv Manuf Tech 102(9-12) (2019) 2907-2918.
[13] M. Zain-Ul-Abdein, D. Nelias, Effect of Coherent and Incoherent Precipitates Upon the Stress and Strain Fields of 6xxx Aluminium Alloys: A Numerical Analysis, Int J Mech Mater Des 12(2) (2016) 255-271.
[14] W. Köster, H. Franz, Poisson's Ratio for Metals and Alloys, Metallurgical Reviews 6(1) (1961).

[15] H.S. Kim, Densification Mechanisms During Hot Isostatic Pressing of Stainless Steel Powder Compacts, J Mater Process Tech 123(2) (2002) 319-322.
[16] B.K. Lograsso, T.A. Lograsso, Examination of Densification of Spherical and Irregular Powders During Hot Isostatic Pressing, Adv Pm Part (1993) 111-125.
[17] J. Thomas, A.F. Bengoa, S.T. Nori, R. Ren, P. Kenesei, J. Almer, J. Hunter, J. Harp, M.A. Okuniewski, The Application of Synchrotron Micro -Computed Tomography to Characterize the Three-Dimensional Microstructure in Irradiated Nuclear Fuel, J Nucl Mater 537 (2020).